B-site cation order/disorder and their valence states in $Ba_3MnNb_2O_9$ perovskite oxide

Yan Xin[a,*], Qing Huang[b], Zahra Shafieizadeh[c], Haidong Zhou[b]

[a] National High Magnetic Field Laboratory, Florida State University, Tallahassee, FL 32310, USA
[b] Department of Physics and Astronomy, University of Tennessee, Knoxville, TN 37996, USA
[c] Department of Physics, Florida State University, Tallahassee, FL 32306, USA

ARTICLE INFO

ABSTRACT

Polycrystalline samples $Ba_3MnNb_2O_9$ synthesized by solid state reaction and single crystal samples grown by optical floating zone have been characterized using scanning transmission electron microscopy and electron energy loss spectroscopy. Three types of B-site Mn and Nb ordering phase are observed: fully ordered 1Mn:2Nb; fully disordered; nano-sized 1Mn:1Nb ordered. No electronic structure change for crystals with different ordering/disordering. The Mn valence is determined to be 2+, and Nb valence is 5+. Oxygen 2p orbitals hybridize with Mn 3d and Nb 4d orbitals. Factors that affect the electron energy loss near edge structures of transition metal white-lines in electron energy loss spectroscopy are explicitly illustrated and discussed.

1. Introduction

Perovskite-related transition metal oxides are among the most intriguing material systems in the field of solid state chemistry and physics. Their physical properties are significantly affected by the changes in chemistry and crystal structure, which is brought about by B-site cation ordering or disordering. Perovskite $Ba(B'_{1/3}B''_{2/3})O_3$ (B = Mn, Ni or Co) is a family of important ceramic materials with desirable dielectric properties suitable for microwave wireless communication applications. In particular, ordered $Ba(B'_{1/3}B''_{2/3})O_3$ or the triple perovskite $Ba_3BNb_2O_9$ has shown multiferroicity [1,2], as photocatalyst [3], and improved microwave dielectric properties [4]. These perovskites can be synthesized by hydrothermal [5], solid state reaction [1,6], aqueous solution [6] and optical floating zone methods. The cation ordering of these perovskites affects their dielectric properties and magnetic ground states. It has been shown that dielectric properties strongly depend on B-site ordering [7]. Using conventional high resolution transmission electron microscopy (HRTEM) imaging and neutron scattering, Liu et al. [6] found that $Ba_3MnNb_2O_9$ samples obtained by solid state reaction are predominately ordered phase; in contrast, samples obtained by aqueous solution are an exclusively disordered phase.

$Ba_3MnNb_2O_9$ is one of the magnetically and geometrically frustrated materials, which has attracted intense research interests in recent years since the inherent spin structure of these materials exhibits new and unusual magnetic phases. The ordered $Ba_3MnNb_2O_9$, for example, is one of a few existing spin 5/2 triangular antiferromagnetic materials. Its negative Curie-Weiss constant suggests a magnetic transition from paramagnetic to antiferromagnetic ordering at 3.5 K [1]. In fact, its two-dimensional triangular lattice with antiferromagnet ordering even shows short-range antiferromagnetic interaction above its Néel temperature T_N [8].

Accurate knowledge of the microstructures and atomic ordering of this material lead to clear understanding of its physical properties, such as its magnetic properties or magnetic ground state. In this paper, we use atomic resolution high-angle-annular-dark-field scanning transmission electron microscopy (HAADF-STEM) imaging techniques to study the order/disorder of Mn and Nb in $Ba_3MnNb_2O_9$ grown by optical floating-zone, also by solid state reaction methods, and use electron-energy-loss-spectroscopy (EELS) core-loss spectrum to investigate the electronic structure and B-site cation valence.

2. Experimental

Two types of samples are studied in this paper. One is polycrystalline samples synthesized by solid state reaction, and the other is single crystal samples grown by optical floating zone (OFZ) method.

For polycrystalline samples, stoichiometric mixtures of $BaCO_3$, Nb_2O_5, and MnO powders were ground together, and pressed into pellets and calcined in air at 1230 °C for 24 h. Single crystal was grown by an optical floating zone furnace, which is equipped with two halogen lamps and double ellipsoidal mirrors. In order to prepare for the single
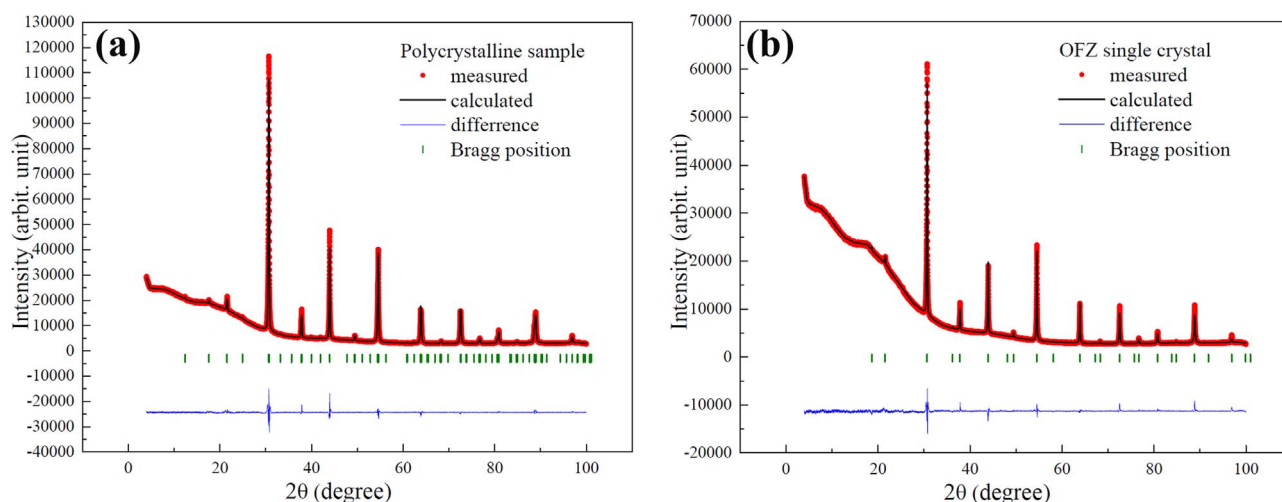
Fig. 1. X-ray diffraction pattern acquired at room temperature from powdered (a) polycrystalline sample; (b) OFZ single crystal.

crystal growth, the polycrystalline sample powder was pressed under 400 atm hydrostatic pressure into feed and seed rods, which were 6 mm in diameter, 60 mm long, and was calcined in Ar gas at 1230 °C for 12 h. The crystal growth, which was controlled at a rate of 10 mm/hour, was carried out in argon gas with feed and seed rods rotating in opposite directions at 25 rpm during growth.

Powder X-ray diffraction data were collected on both powdered polycrystalline and OFZ single crystal samples at room temperature using Cu Kα1 radiation (λ = 1.54051 Å). The data were analyzed using the Rietveld refinement method. Magnetic susceptibility of the OFZ single crystal sample was measured as a function of temperature using a SQUID magnetometer. For SQUID measurements, the sample was cooled in zero field to 2 K; then the susceptibility data was taken while warming the sample to 300 K in a 1 T magnetic field.

TEM samples were prepared by crushing samples in ethanol with a mortar and pestle. Subsequently, this ethanol suspension of crushed crystals was dropped with a pipette onto a 200 μm mesh TEM copper grid which is coated with a holey carbon film.

STEM study was carried out on a probe-aberration-corrected, cold-field-emission JEM JEOL-ARM200cF at 200 kV, equipped with a Gatan Orius camera, a JEOL HAADF-STEM detector and a Gatan GIF Quantam963 with DualEELS capability. The STEM resolution is 0.078 nm, and energy resolution is 0.5 eV at full emission.

HAADF-STEM images were acquired using a spot size 7c, 30 μm condense lens aperture, at an image scan speed of 32 μs/pixel. The beam convergent angle was 21 mrad, and the STEM image collection angle was from 68 mrad to 174 mrad. Core-loss EELS spectra for Mn, Nb, and O were collected to investigate the valence and electronic structure of samples with different B-site ordering. They were collected in TEM diffraction mode at 8 cm camera length with a 2.5 mm slit at an energy dispersion of 0.1 eV. The electron beam was focused into a crystal area of about 80–100 nm in diameter. The convergence angle is 7.6 mrad and EELS collection angle 17.4 mrad. Each core-loss spectrum was acquired in 2 s using DualEELS, which enables zero loss peak (ZLP) to be simultaneously collected with core-loss spectrum.

Several crystal pieces were studied for each different phase. For each crystal piece with size of roughly 1−2 μm, about 9 spectra were collected. Although we found no difference in energy-loss-near-edge structure (ELNES) between spectra taken from different crystal orientations, all core-loss spectra were taken along the same crystal orientation for easy comparison. Before we started acquiring each individual EELS spectrum, we first deleted the spectrometer dark current background file so that a new dark current background would be automatically acquired for each spectrum, thus avoiding a fixed noise pattern. We examined the sample area after each individual

spectrum was taken to ensure that the EELS data were collected on pristine crystal without any beam damage.

3. Results and discussion

3.1. X-ray diffraction and magnetic property

The Rietveld refinement of room temperature X-ray diffraction from powdered crystals (Fig. 1a and b) has identified two crystal phases. The polycrystalline sample has an ordered B-sites phase (Table 1). For the ordered phase, the standard formula is $Ba_3MnNb_2O_9$, where the Mn and Nb sites have the ordering of 1Mn:2 Nb (−Mn-Nb-Nb-Mn-Nb-Nb-....). This material is a triple perovskite, has a P-3m1 trigonal structure, and lattice parameters of a = 0.5816 nm and b = 0.7146 nm, in agreement with what was reported before [1,9].

For the OFZ single-crystal sample, the best refinement model is $Ba_2(Mn_{2/3}Nb_{1/3})NbO_6$, which has a cubic structure with Fm-3m symmetry and a lattice parameter of 0.8235 nm (Table 2). This structure is not completely randomly disordered with 1/3Mn : 2/3Nb on all the B-sites, since some B-site has mixed Mn and Nb, and some sites just have Nb. However, the calculated pattern from this model shows two peaks at 18° and 36°, which are missing from the experimental pattern. But for a completely disordered B-site phase, $Ba(Mn_{1/3}Nb_{2/3})O_3$ that has a higher symmetry, leads to the absence of these two Bragg peaks. This uncertainty by X-ray diffraction modeling is related to the TEM observation shown below as the OFZ single crystal has a disordered matrix with nano-sized ordered phases.

The temperature dependence of molar magnetic susceptibility of

Table 1
Refined structural parameters of polycrystalline sample.

Polycrystal sample a = b = 5.81563(4) Å, c = 7.14604 (6) Å, overall B factor = 0.13405 Å² Space group: P-3m1					
Atom	Site	X	Y	Z	Occ.
Ba1	2d	0.3333	0.6667	0.6656	0.16667
Ba2	1a	0	0	0	0.08333
Mn	1b	0	0	0.5	0.08333
Nb	2d	0.3333	0.6667	0.1671(4)	0.16667
O1	3e	0.5	0	0	0.25
O2	6i	0.1859(7)	0.3717(14)	0.2726(4)	0.5
Bond distance(Å)					
Nb-O1	2.060(1)				
Nb-O2	1.666(3)				
Mn-O2	2.479(3)				

Table 2
Refined structural parameters of single-crystal sample.

Single crystal sample a = b = c = 8.23518 (3) Å, overall B factor = 0.48341 Å^2 Space group: Fm-3m					
Atom	Site	X	Y	Z	Occ.
Ba	8c	0.25	0.25	0.25	0.04167
Nb1	4a	0	0	0	0.00695
Mn	4a	0	0	0	0.01389
Nb2	4b	0.5	0.5	0.5	0.02084
O	24e	0.274(1)	0	0	0.125
Bond distance(Å)					
Nb-O	1.862(10)				
Nb$_{1/3}$Mn$_{2/3}$-O	2.256(10)				

the polycrystalline sample and the OFZ single crystal sample are shown in Fig. 2. The polycrystalline sample shows an antiferromagnetic transition at 3.2 K (Fig. 2a, reproduced from Ref. [1]). However, the OFZ single crystal shows paramagnetic behavior and does not show antiferromagnetism in this temperature range. The data in the temperature range of 20–300 K were fitted to the Curie-Weiss plot. A Weiss constant of −29.2 K and a Curie constant of 4.832 are obtained for the single-crystal sample, which is comparable to −26 K and 4.305 for the polycrystalline sample [1]. This negative Weiss constant is indicative of antiferromagnetic interactions between the Mn ions [26]. It is interesting that magnetic susceptibility of both samples has very similar temperature dependence from 20K to 300K, indicating similar magnetic interactions.

3.2. Microstructures by atomic resolution HAADF-STEM

Microstructures of Ba$_3$MnNb$_2$O$_9$ crystals such as twins and stacking faults have been observed by conventional TEM [6]. A stacking fault model has been proposed [10], but not confirmed by extensive image simulation. HRTEM images from a field emission microscope have a complex pattern of contrast that varies considerably with image defocus and sample thickness, therefore difficult to interpret. Here we use atomic resolution HAADF-STEM to study the microstructures of both polycrystalline and OFZ single-crystal samples. The HAADF-STEM provides direct structural information at an atomic scale that is easy to interpret with no need for image simulation. The atomic columns in the image shown as bright spots against dark background, which is sensitive to atomic number Z. Since the atom intensity is proportional to Z^n [11], Ba, Mn, and Nb atomic columns in our samples are readily distinguishable based on their atomic column intensity in the HAADF-STEM images.

3.2.1. B-site order and disorder

The best orientation to check the B-site ordering is to view along $< 110 >_c$ of the cubic perovskite unit cell, which are shown in Fig. 3a and b, where the c means the indexing from a cubic cell. In this projection, the B-site atoms, Mn and Nb, are sandwiched between the Ba atomic planes. For ordered Ba$_3$MnNb$_2$O$_9$ phase, Mn and Nb are ordered, where they form …–Mn-Nb-Nb-… ordering on {111}$_c$ plane. The HAADF-STEM Z-contrast image of ordered crystal shows distinctly alternating low-high-high intensity, where Mn is the lowest intensity columns, and Nb columns have higher intensity (Fig. 3c). An intensity profile of this atomic plane (insets) confirms very clearly the …-Mn-Nb-Nb-…. ordering. For a crystal with perfect 1Mn:2 Nb ordering, the electron diffraction is shown in Fig. 3e, where there are two sharp and bright diffraction spots along $< 111 >_c$ direction at 1/3 and 2/3 of {111}$_c$.

For the polycrystalline sample, the majority crystals are the ordered phase, while crystals with disordered B-site are also found. For disordered phase, the B-site cation has random distributed Mn and Nb atoms. Each B-site atom has 1/3 Mn and 2/3 Nb on average, which corresponds to an average atomic number 39. Therefore in the HAADF-STEM Z-contrast image (Fig. 3d), the brighter atomic column are Ba atom column (Z = 56), and the lower intensity atomic column are mixed Mn and Nb, showing similar column intensity. The characteristic feature for the disordering is also reflected in electron diffraction pattern of the crystal (Fig. 3f), where there is no diffraction spots or any intensity between (000) and {111}$_c$ diffraction spots along $< 111 >_c$ direction. Although it's hard to detect disordered phase in the polycrystalline samples by X-ray diffraction, TEM observation reveals that there are disordered crystals in the majority-ordered polycrystalline samples.

3.2.2. New type of B-site cation ordering in OFZ single crystal

HAADF-STEM easily reveals B-site ordering, in addition to its FFT and its inverse FFT by the superlattice diffractions (Fig. 4). In particular, in the inverse FFT, Mn atoms show as black spots, while the Nb atoms are the white dots with the 1Mn:2Nb ordering. Through image processing, the ordering of Mn and Nb showed more pronounced contrast (Fig. 4d) by adding the inverse FFT image to the original STEM image. A new type of B-site ordering is shown in Fig. 4e-h. The intensity profile of Mn-Nb plane has a low and a high alternating intensity variation (Fig. 4e). The inverse FFT image shows ordering of one black and one white dots, which are Mn and Nb with 1Mn:1Nb ordering. This new ordering also reflected in the FFT diffraction pattern with one superlattice spot at ½{111}$_c$ (Fig. 4f).

Nanometer-sized pockets of different ordered regions were found embedded in the mostly disordered OFZ single crystal sample. A larger view-area (Fig. 5a) clearly show high density of 2–4 nm sized 1Mn:1 Nb
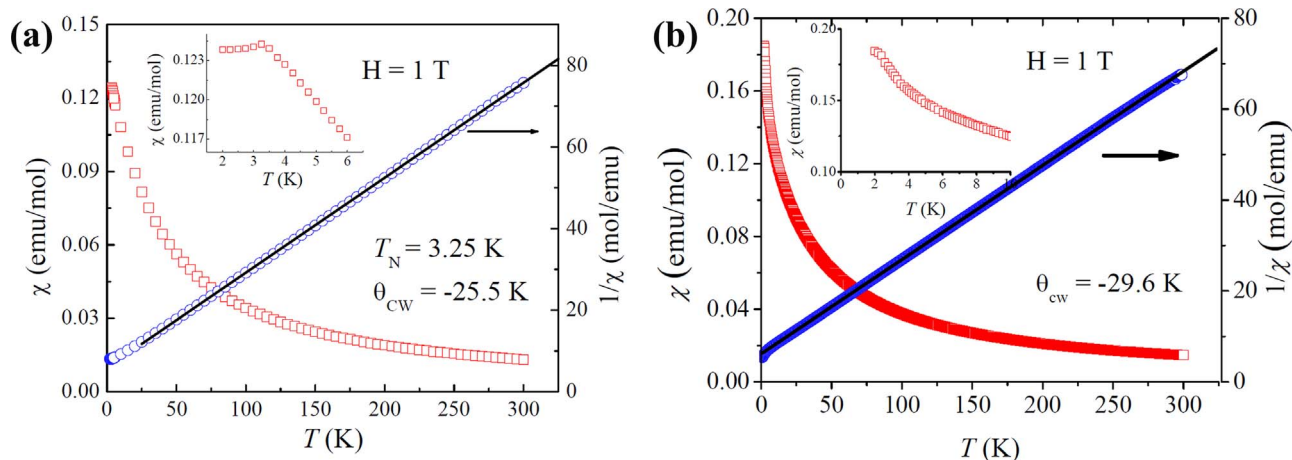
Fig. 2. Molar magnetic susceptibility of (a) powdered polycrystalline samples [1]; (b) OFZ single crystals, and their corresponding linear Curie-Weiss law fitting. The insets are the enlarged low temperature part.
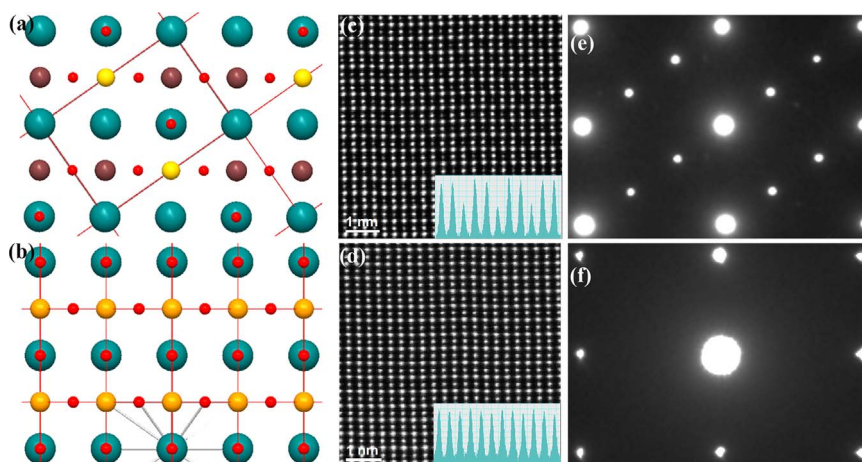
Fig. 3. (a) Schematic view of the ordered structure looking down < 110 > $_c$; (b) Schematic view of the disordered structure; (c) HAADF-STEM image of the ordered structure of polycrystalline sample and (d) disordered along < 110 > $_c$ with inset showing intensity line profile of Mn-Nb plane of polycrystalline sample; (e) < 110 > $_c$ electron diffraction pattern of ordered phase in polycrystalline sample; (f) < 110 > $_c$ electron diffraction pattern of disordered phase of polycrystalline sample.
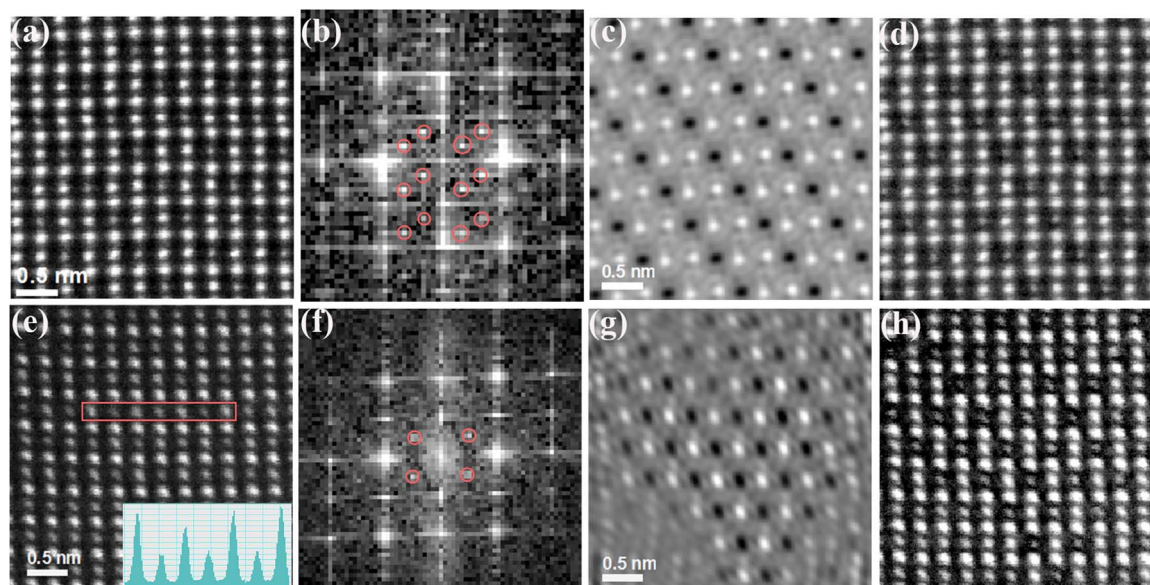

Fig. 4. (a) original HAADF-STEM image of a 1Mn:2Nb ordered region along < 110 > $_c$ of polycrystalline sample; (b) FFT of (a); (c) inverse FFT image using the $1/3\{111\}_c$ and $2/3\{111\}_c$ superlattice spots that are indicated by the circles; (d) processed HAADF-STEM image of (a) showing more pronounced ordering contrast; (e) original HAADF-STEM image of a 1Mn:1Nb ordered region along < 110 > $_c$ of single-crystal sample; inset: line intensity profile of Mn-Nb plane; (f) FFT of (e) showing the $1/2\{111\}_c$ superlattice spots; (g) inverse FFT image using the $1/2\{111\}_c$ superlattice spots; (h) processed HAADF-STEM image of (e) showing more pronounced contrast of 1Mn:1Nb ordering.

ordered phase domains and some 1Mn:2Nb ordered domains embedded in the disordered matrix. It should be noted that the disordered matrix surrounding the small domains of the ordered phase makes atomic column intensity ratio between Mn and Nb lower than what would be for ratio between pure Mn and pure Nb columns. FFT diffraction pattern (Fig. 5b) and the selected area electron diffraction pattern from about 0.5 μm diameter area of a single crystal, both exhibit sharp ordering diffraction spots at ½ $\{111\}_c$ and diffused streaks at 1/3 and 2/3 of $\{111\}_c$ (Fig. 5c). This indicates that new 1Mn:1Nb order is three dimensional inside the disordered matrix. In addition to this 1Mn:1Nb new phase, the 1Mn:2Nb ordered phase is also present in forms of random platelets on all $\{111\}_c$ planes, evidenced by the broad diffuse streaks (Fig. 5b). From these observations, it is confirmed that we discovered a new ordered phase in OFZ single crystal sample as the 1Mn:1Nb ordering, −Mn-Nb-Mn-Nb-.

3.2.3. Domains

We have observed boundaries between two ordered domains and between ordered and disordered domains in the polycrystalline sam-

ples. The domain boundary between two ordered domains is shown in Fig. 6. The ordered domain may nucleate on any of the four $\{111\}_c$ planes, which could result in multi-domain configurations in ordered crystals. The selected area diffraction pattern of a double-domain crystal is exhibited in Fig. 6a. The two ordered domains have the 1Mn:2Nb ordering on two sets of $\{111\}_c$ planes. They can be identified by either HAADF-STEM images or its FFT. The domain boundary is about 5 nm thick (Fig. 6b). At the domain boundary (Fig. 6c), atomic column intensity of the Mn-Nb planes has a certain repeating pattern: atomic layer1 has one dark followed by two bright columns; atomic layer 2 and 3 have an intensity pattern of one brighter followed by two darker columns. This can be explained by overlapping of two sets of ordered $\{111\}_c$ planes shown in the sketch. For atomic layer1, the lowest intensity columns are the pure Mn column, and the two bright columns are pure Nb columns. For atomic layers 2 and 3, the brightest columns are Nb columns, and the weaker ones are mixed Mn and Nb columns. So the domain wall region is the overlap between the two domains. In a cubic structure, there are four equivalent $\{111\}$ planes, on which 1Mn:2Nb ordering can form. From the observed domain
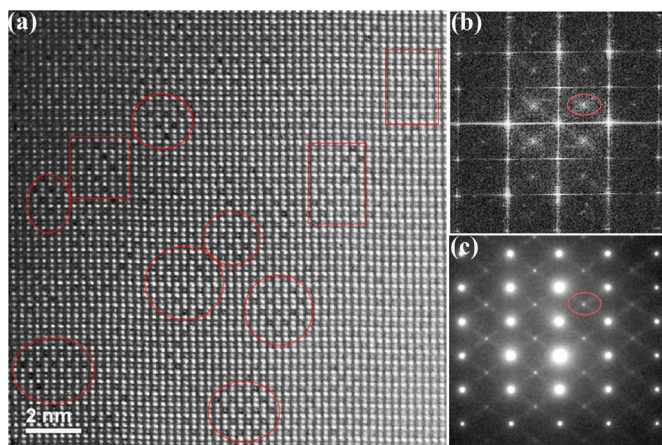
Fig. 5. (a) processed HAADF-STEM image of a larger area from OFZ single-crystal sample with different ordering indicated: circles are 1Mn:1Nb ordered domains; square or rectangle frames are 1Mn:2Nb ordered platelets. (b) FFT of (a) showing sharp $\frac{1}{2}\{111\}_c$ superlattice spots and diffused $1/3\{111\}_c$ and $2/3\{111\}_c$ streaks; (c) $<110>_c$ electron diffraction pattern from a large OFZ single crystal piece.

configurations, we speculate that the 1Mn:2Nb ordered domains nucleated inside the disordered cubic crystal, and they grew bigger in size and density with time at the elevated temperature.

Some of the polycrystalline pieces have both ordered and disordered regions. The domain boundary of ordered and disordered region is smooth with no disruption of the structure as shown in Fig. 7. The boundary is not all atomically sharp. It expands a few atomic layers, depending on how the ordering ends, and how the disordering starts. The TEM observations revealed that there are a certain amount of disordered regions/crystals in polycrystalline samples, which is not easily detected by X-ray diffraction. Longer reaction time at 1230 °C might increase the percentage of the ordered phase.
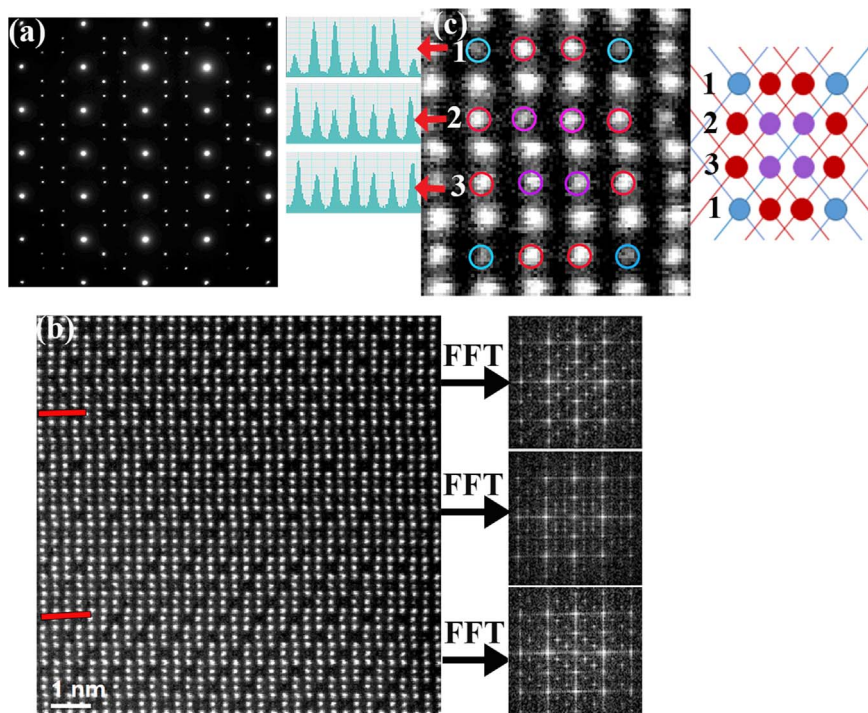
3.3. B-site cation valence and electronic structure by core-loss EELS

EELS in TEM, with its very high spatial resolution, is a unique tool to study the local electronic structure and chemical bonding such as the oxidation states of metallic elements in transition metal oxides. Core-loss EELS probes the unoccupied density of states in conduction bands above the Femi level. Notably, the energy loss near edge structures (ELNES) provides information about electronic structures. Mn valence in oxides has been extensively studied using its white-lines, L_2 and L_3 [12–17], which are transitions from $2p^{3/2}$ and $2p^{1/2}$ to unoccupied states in $3d^5$ orbitals respectively. Since Mn $2p^{3/2}$ and $2p^{1/2}$ hybridize with oxygen 2p orbitals, the L_2 and L_3 intensity ratio has been used to quantitatively determine the valence state of Mn in bulk or at interfaces in thin films of Mn-containing oxides [16,18]. Additionally, the difference in ELNES relative peak heights have been used as evidence for chemical bonding change between different phases or different temperatures [19,20].

Here, we first discuss the uncertainty in $L_{2,3}$ ELNES, i.e. the relative L_2, and L_3 peak height. Factors that make the $L_{2,3}$ relative peak height appear different are background window position, background window width, sample thickness, and spectrometer noise, as shown in Fig. 8. Backgrounds of the spectra are subtracted using a power law fit in the DigitalMicrograph software. Fig. 8a and b show significant effect of background window width and position on the $L_{2,3}$ relative peak height. Therefore, when comparing peak height, it is advised to use the same window position and width for background subtraction for every spectrum. Sample thickness also influences the relative $L_{2,3}$ peak heights, as shown in Fig. 8c. Therefore, plural scattering must be removed from the spectrum using Fourier-Ratio deconvolution method. Even after exactly the same background subtraction and plural scattering removal, as shown in Fig. 8d, two Mn $L_{2,3}$ core loss spectra taken from the same crystal shows difference when normalized to L_2 peak. However, if the spectrum is normalized to L_3, the difference in peak height is within the statistic noise of the background, indicating no relative peak height difference. Since there should be no valence change as the two spectra were from the perfect region of the same
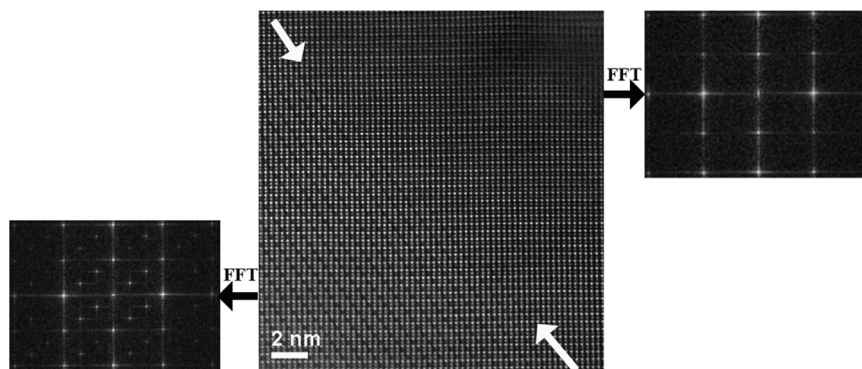

Fig. 6. (a) Selected area electron diffraction pattern of two ordered domains from polycrystalline sample; (b) HAADF-STEM image of order/order domain from polycrystalline sample; FFT diffraction patterns from top, middle and bottom region; (c) blown up of the domain boundary with line intensity profiles of Mn-Nb plane; the sketch shows the $\{111\}_c$ Nb planes (red line) and $\{111\}_c$ Mn planes (blue line) intersect at the domain boundary forming pure Nb columns (red), pure Mn columns, and mixed Mn/Nb columns (purple);.

Fig. 7. HAADF-STEM image of the boundary between ordered and disordered region of polycrystalline sample. Top right: FFT from the disorder region; Bottom left: FFT from the ordered region.
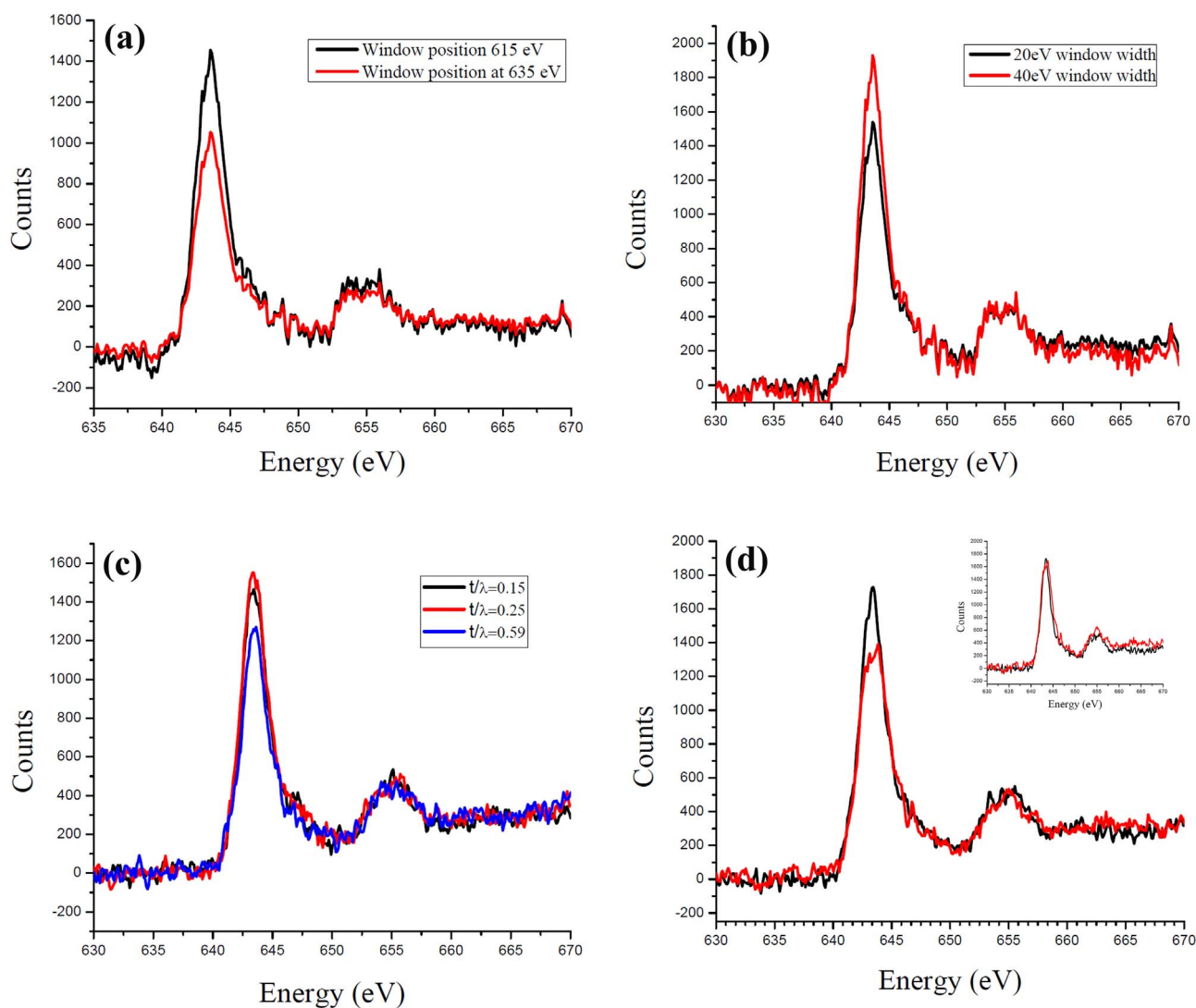

Fig. 8. Superimposed Mn $L_{2,3}$ spectra from the same crystal piece of ordered polycrystalline sample after normalized to L_2: (a) the same spectrum processed using different background window position; (b) the same spectrum using different background window width; (c) from different sample thickness; (d) after the same processing. Inset: normalized to L_3.

crystal, the difference in L_3 peak height shown in Fig. 8d is not real, and not related to valence change.

There is a wealth of literature that uses $I(L_3)/I(L_2)$ to determine Mn valence, for example, Ref. 12–18. We use Hartree-Slater (HS) cross section function in DigitalMicrograph to process our $L_{2,3}$ EELS spectra [16]. After normalizing the HS background to the continuum back-

ground at the high energy end of L_2 peak (from 657 to 665 eV), the peak intensities are obtained by integrating spectrum from 637 to 645 eV for L_3 peak, and from 648 eV to 656 eV for L_2 peak after subtracting HS background. For the 9 spectra collected from the same crystal pieces, the $I(L_3)/I(L_2)$ ratios are shown in Fig. 9a. The variation of this ratio stems from statistical uncertainties consistent with the
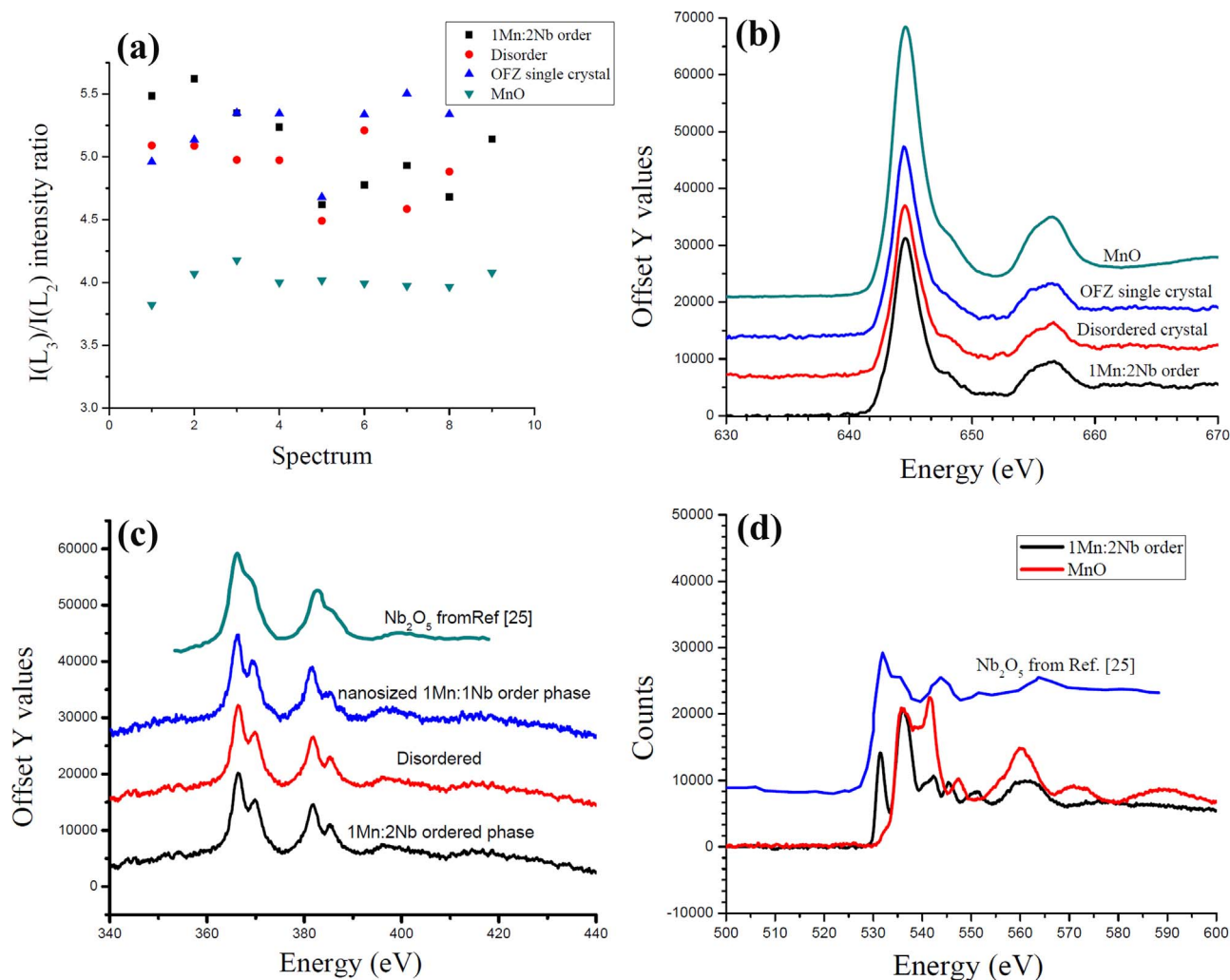
Fig. 9. (a) Plot of Mn $L_{2,3}$ white-line intensity ratio $I(L_3)/I(L_2)$, summarized from 8 to 9 spectra for each phase, together with control sample MnO; (b) Mn $L_{2,3}$ from three phases and from reference sample MnO; (c) Nb $M_{2,3}$ spectrum from three phases; and from Ref. [25]; (d) O-K core loss of $Ba_3MnNb_2O_9$ superimposed with O-K spectrum of MnO and Nb_2O_5 from Ref. [25].

spectrum error proposed by Riedl et al. [21]. Based on this observation, when studying two different phases with the same experimental settings, it would be incorrect to claim valence change if the variation was within this statistical uncertainty. Therefore to evaluate valence changes, it is recommended that the same background subtraction (the same window width and position) and plural scattering removal method is used for each spectrum. In addition, the statistical uncertainty in $I(L_3)/I(L_2)$ should be measured by taking multiple spectra in nominally identical conditions.

We compare Mn $L_{2,3}$, Nb $M_{2,3}$ and O-K edge spectra obtained from 1Mn:2Nb ordered, disordered, and nano-sized 1:Mn:1Nb ordered in disordered matrix crystals. All spectra were taken along $< 110 >_c$ orientation under exactly the same experimental conditions. A reference spectrum of Mn^{2+} was obtained from a commercial MnO powder sample (Alfa Aesar 99.99%). All spectra were calibrated using their corresponding ZLP. The spectra were processed using following parameters: background windows are 20 eV before the onset of each peak, which is 635 eV for Mn, 320 eV for Nb, and 514 eV for O. To increase the statistical accuracy, 9–18 spectra are summed up (Fig. 9b-d). No difference was observed among three different phases, suggesting no valence or other electronic structure change due to Mn and Nb ordering or disordering.

For Mn, $I(L_3)/I(L_2)$ ratio are calculated for several spectra taken from each phase and plotted in Fig. 9a. The ratios are 5.09 ± 0.36 for

1Mn:2Nb ordered, 4.91 ± 0.25 for disordered, and 5.21 ± 0.27 for the nano-sized 1Mn:1Nb/disordered matrix. Evidently, there is no $I(L_3)/I(L_2)$ difference within the measurement error. In contrast, $I(L_3)/I(L_2)$ of MnO $L_{2,3}$ ratio is 4.01 ± 0.10, significantly lower than that of the Ba-compounds, indicating a less occupied d states [14]. Also, no Mn L_3 chemical shift for all three phases is observed with respect to the Mn L_3 peak in MnO. The Mn $L_{2,3}$ ELNES shows L_3 with one major peak and a small shoulder on the higher energy side, and L_2 can be fitted into two peaks with the same height (Fig. 9b), which are the same as MnO, a typical $3d^5$ system [22]. The ELNES peak shape suggests that it has a high-spin ground state of $S_{5/2}$, not a low spin state [23]. So it is likely that Mn in these Ba-compounds has a valence state 2+ with a high-spin state regardless of its ordering/disordering. The bond lengths of the Mn-O octahedron varies slightly depending on its ordering; the Mn^{2+} ELNES are not sensitive to the slight change in bond length [24].

Nb $M_{2,3}$ spectra from the three phases are presented in Fig. 9c. They have the same ELNES of double-peak structures, similar to the ELNES of Nb^{5+} in Nb_2O_5 [25]. The ELNES of O-K are also very similar for three phases, which have two pronounced peaks within 7 eV of the O-K onset (Fig. 9d). By comparing with that of MnO, and the O-K ELNES from Nb_2O_5 [25], it is reasonable to speculate that the two peaks within 7 eV of the onset in these Ba-compounds are hybridization of oxygen 2p orbitals with Mn 3d and Nb 5d. Nb^{+5} may contribute electrons to oxygen 2p orbitals, due to the extended Nb 5d electrons in

the p-d orbital interaction with oxygen, which leads to more filled d states for Mn^{+2} electrons, so that the Mn $I(L_3)/I(L_2)$ ratio is moderately higher than that of MnO.

4. Conclusions

We found three types of ordering/disordering in these Ba-Mn-Nb-O compounds: a 1Mn:2Nb ordered (-Mn-Nb-Nb-), a 1Mn:1Nb nanometer-sized ordered (-Mn-Nb-), and a Mn and Nb completely disordered. There are a certain amount of disordered crystals in the ordered $Ba_3MnNb_2O_9$ polycrystalline samples. Ordered/ordered and ordered/disordered domains are observed to be present in one single crystal piece. Atomic resolution HAADF-STEM imaging clearly reveals atomic structure of the domain boundary. Four ordered domains can form on different $\{111\}_c$ planes in one crystal. The single crystals grown by optical floating zone does not show antiferromagnetism but has high negative Weis constant, similar to the polycrystalline samples. Transition metal $L_{2,3}$ core-loss white-line relative peak height is affected by EELS background subtraction, sample thickness, and signal noise. Their relative peak height difference should not be used as evidence for valence change if the difference of their intensity ratio is within statistical error. The Mn has 2+ valence, and Nb has 5+ valence for all three phases. The $L_{2,3}$ white line ratio of Mn in these oxides has larger value than that of typical MnO due to the contributed Nb^{5+} electrons.

Acknowledgements

References

[1] M. Lee, E.S. Choi, X. Huang, J. Ma, C.R. Dela Cruz, M. Matsuda, W. Tian, Z.L. Dun, S. Dong, H.D. Zhou, Phys. Rev. B 90 (2014) 224402.
[2] J. Hwang, E.S. Choi, F. Ye, C.R. Dela Cruz, Y. Xin, H.D. Zhou, P. Schlottmann, Phys. Rev. Lett. 109 (2012) 257205.
[3] B. Xu, F. Zhang, X.Y. Liu, J.H. Ye, W.H. Zhang, L. Shi, X.G. Wan, J. Yin, Z.G. Liu, Phys. Rev. B 76 (2007) 125109.
[4] I. Molodetsky, P.K. Davies, J. Euro, Ceram. Soc. 21 (2001) 2587–2591.
[5] A. Dias, V.S.T. Ciminelli, F.M. Matinaga, R.L. Moreira, J. Eur. Ceram. Soc. 21 (2001) 2739–2744.
[6] Y. Liu, R.L. Withers, A.P. Whichello, L. Noren, V. Ting, F. Brink, J.D. Fitz Gerald, J. Sol. Stat. Chem. 178 (2005) 3389–3395.
[7] R.J. Cava, J. Mat. Chem. 11 (2001) 54–62.
[8] Zhaoming Tian, Qian Guo, Zhongwen Ouyang, Guihuan Du, Wei Tong, Junfeng Wang, Songliu Yuan, Sol. Stat. Com. 191 (2014) 66–69.
[9] U. Treiber, S. Kemmler Sack, J. Sol. Stat. Chem. 43 (1982) 51–62.
[10] Y. Liu, R.L. Withers, V. Ting, J.D. FitzGerald, L. Noren, Phys. B 385–386 (2006) 564–566.
[11] S.J. Pennycook, L.A. Boatner, Nat 336 (1988) 565–567.
[12] J.H. Rask, B.A. Miner, P.R. Buseck, Ultra 21 (1987) 321–326.
[13] J.H. Paterson, O.L. Krivanek, Ultra 32 (1990) 319–325.
[14] Hiroki Kurata, C. Colliex, Phys. Rev. B 48 (1993) 2102–2108.
[15] H.K. Schmid, W. Mader, Micron 37 (2006) 426–432.
[16] M. Varela, M.P. Oxley, W. Luo, J. Tao, M. Watanabe, A.R. Lupini, S.T. Pantelides, S.J. Pennycook, Phys. Rev. B 79 (2009) (085117-14).
[17] Haiyan Tan, Jo Verbeeck, Artem Abakumov, Gustaaf Van Tendeloo, Ultra 116 (2012) 24–33.
[18] L. Laffont, P. Gibot, Mater. Character 61 (2010) 1268–1273.
[19] Ø. Prytz, E. Flage-Larsen, L. Gu, W. Sigle, P.A. van Aken, J. Taftø, Phys. Rev. B 85 (2012) 195112.
[20] M.J. Neish, M.P. Oxley, J. Guo, B.C. Sales, L.J. Allen, M.F. Chisholm, Phys. Rev. Lett. 114 (2015) 106101–106106.
[21] T. Riedl, T. Gemming, K. Wetzig, Ultra 106 (2006) 284–291.
[22] Frank de Groot, Akio Kotani, Core Level Spectroscopy of Solids, CRC press, Taylor and Francis Group, 2008, p. 241.
[23] S.P. Cramer, F.M.F. de Groot, Y. Ma, C.T. Chen, F. Sette, G. Kipke, S. Brooker, V. Mckee, O.C. Mullins, J.C. Fuggle, J. Am. Chem. Soc. 113 (1991) 7937–7940.
[24] L.A.J. Garvie, A.J. Craven, Phys. Chem. Min. 21 (1994) 191–206.
[25] David Bach, Reinhard Schneider, Dagmar Gerthsen, Jo Verbeeck, Wilfried Sigle, Microsc. Microanal. 15 (2009) 505–523.
[26] Asato Mizuno, Yoshiaki Shuku, Michio M. Matsushita, Masahisa Tsuchiizu, Yuuki Hara, Nobuo Wada, Yasuhiro Shimizu, Kunio Awaga, Phys. Rev. Lett. 119 (2012) 057201–057206.